Supporting Information

$Zn_{3-x}H_{2x}(OH)_2(MoO_4)_2 \bullet H_2O$: A crystallographically accurate Φ_y-type structure of "$Zn_5Mo_2O_{11} \bullet 5H_2O$"

Paul F. Smith[a], Logan Kiesewetter[a], Cheyann Odle[a], the smSFX collaboration[b], Joyce Pham[c]

[a.] *Department of Chemistry, Valparaiso University, 1710 Chapel Drive, Valparaiso IN, USA.*
[b.] *Linac Coherent Light Source, SLAC National Accelerator Laboratory, Menlo Park, CA, USA*
[c.] *Department of Chemistry and Biochemistry, California State University, San Bernardino, San Bernardino CA 92407, USA*

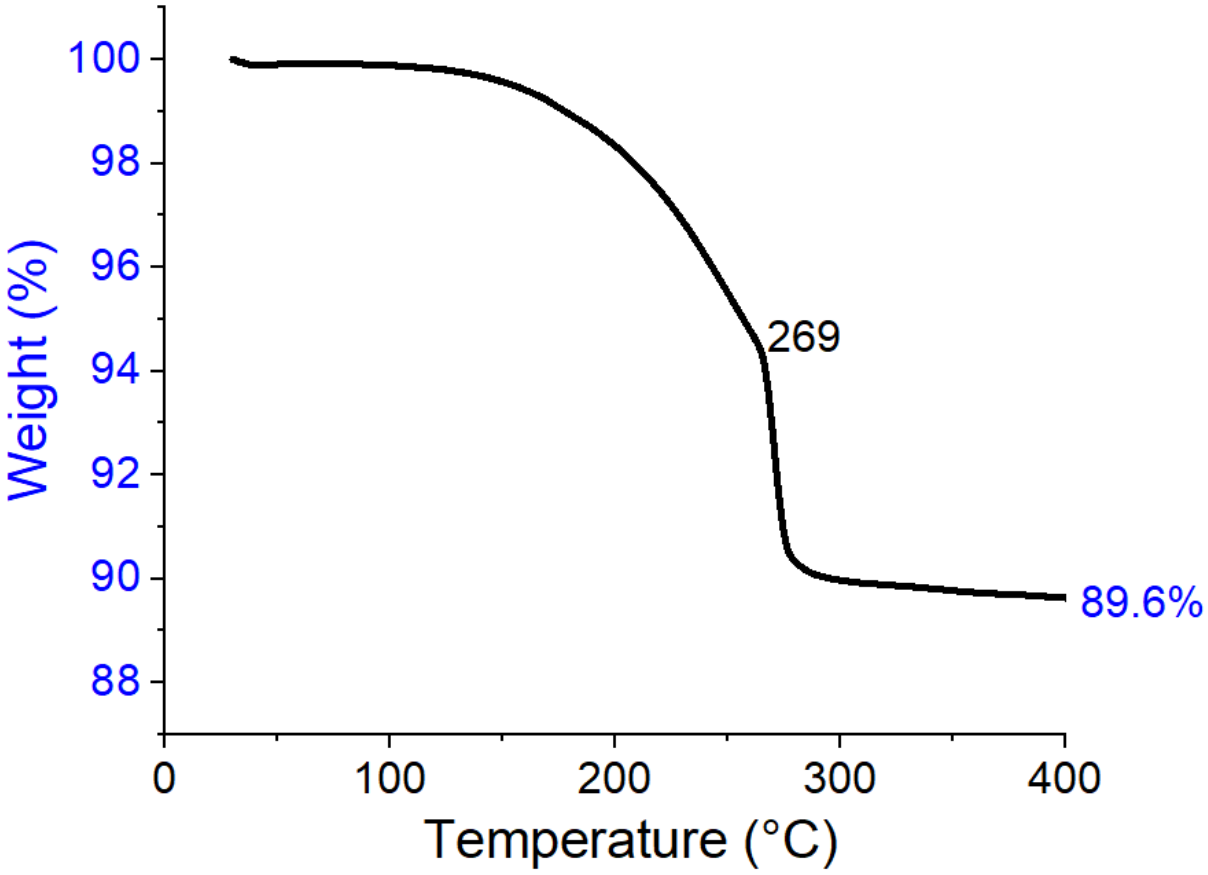

SI Figure 1. Thermogravimetric analysis of **1.** The theoretical mass lost as water from $Zn_3(OH)_2(MoO_4)_2 \bullet H_2O$ is 6.8%. Weight loss below 200°C is reversible and nondestructive to the crystal structure and therefore is assigned to adsorbed water.

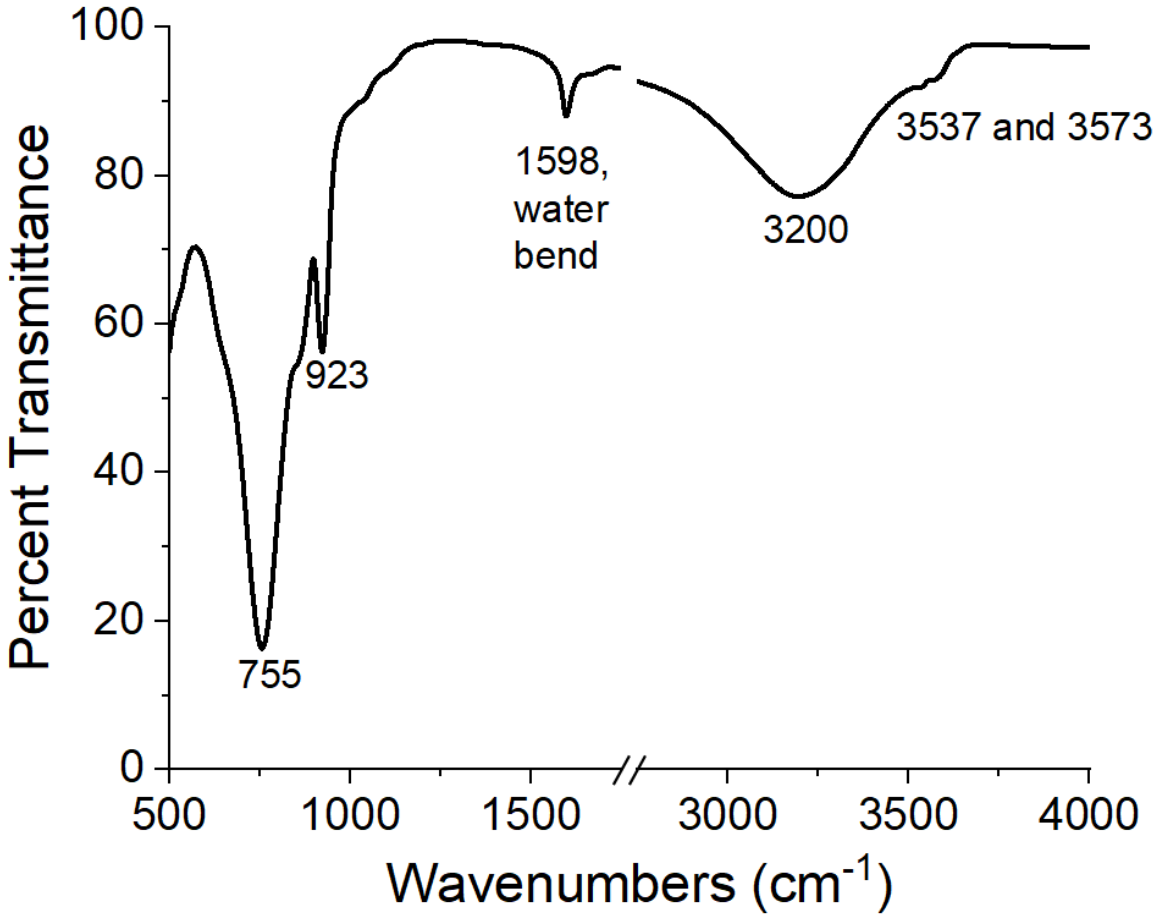

SI Figure 2. Room temperature IR spectrum of **1**.

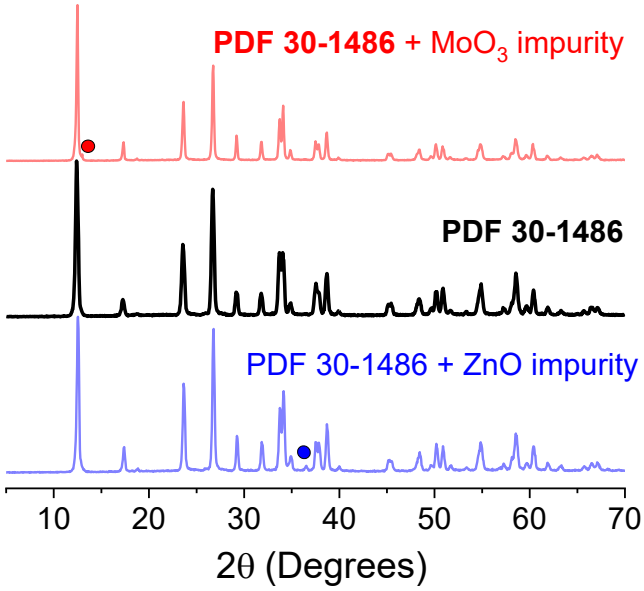

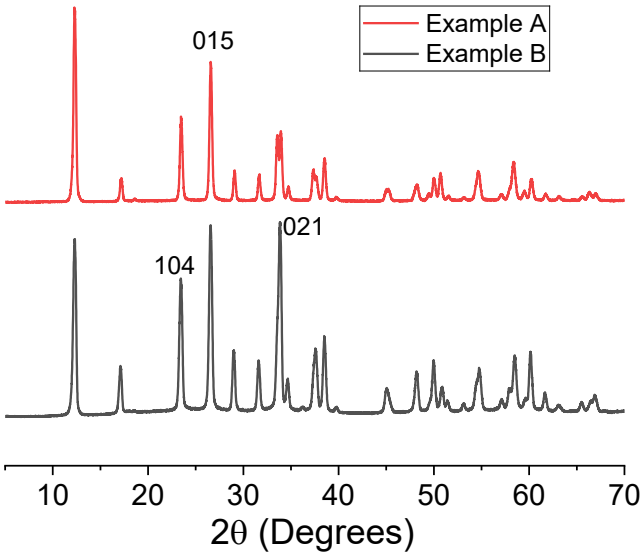

SI Figure 3. (Top) An example of synthesis. 1.28 g of ZnO and 1.80 g of MoO_3 are combined in 400 mL of water and stirred for 6 hours. A portion is filtered and dried for analysis by PXRD, yielding one of the three above patterns. If $MoO_3 \bullet 2H_2O$ is detected (red trace), ZnO is added to the synthesis; vice versa for detection of ZnO (blue trace). This process is repeated until the pattern matches PDF 30-1486 (black). (Bottom): An example of two preparations showing different relative intensities and hkl labels. The different hkl intensities especially of 015 can also be seen in the top image.

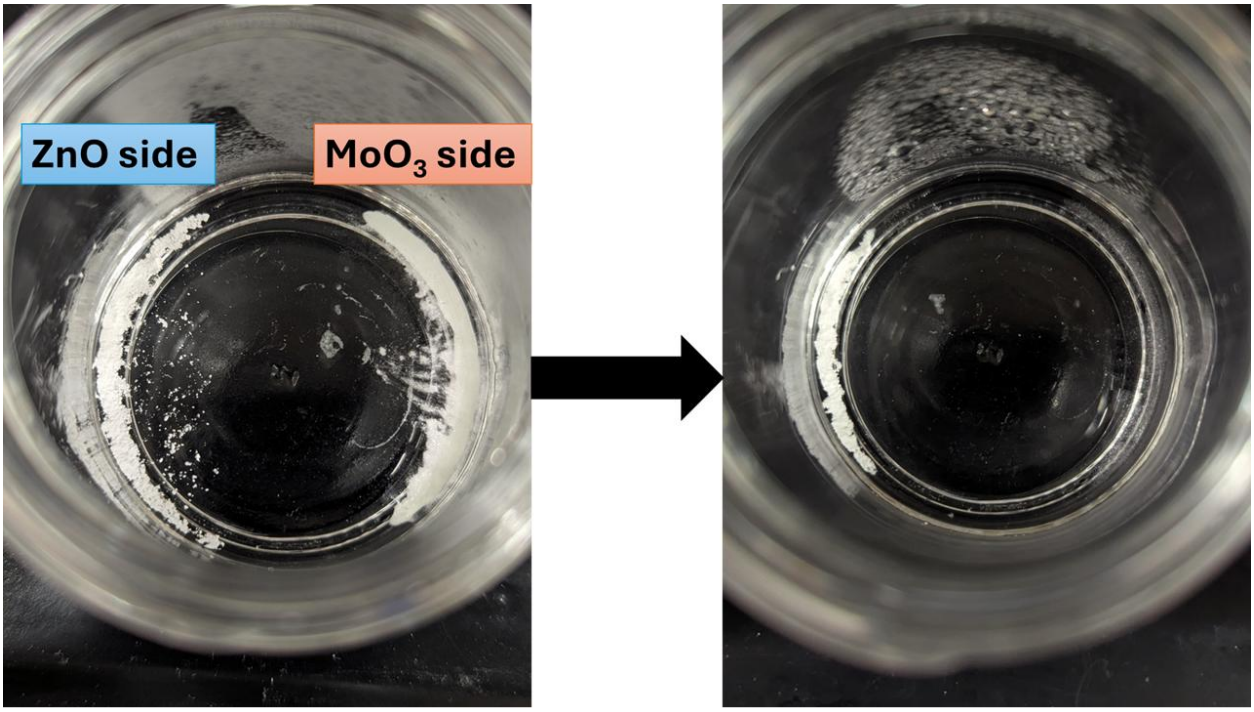

SI Figure 4. Samples prepared without stirring ZnO and MoO_3, which initially begin the reaction in an indented glass vessel. Over time, the MoO_3 side disappears, and the product on the ZnO side analyzes as PDF 30-1486.

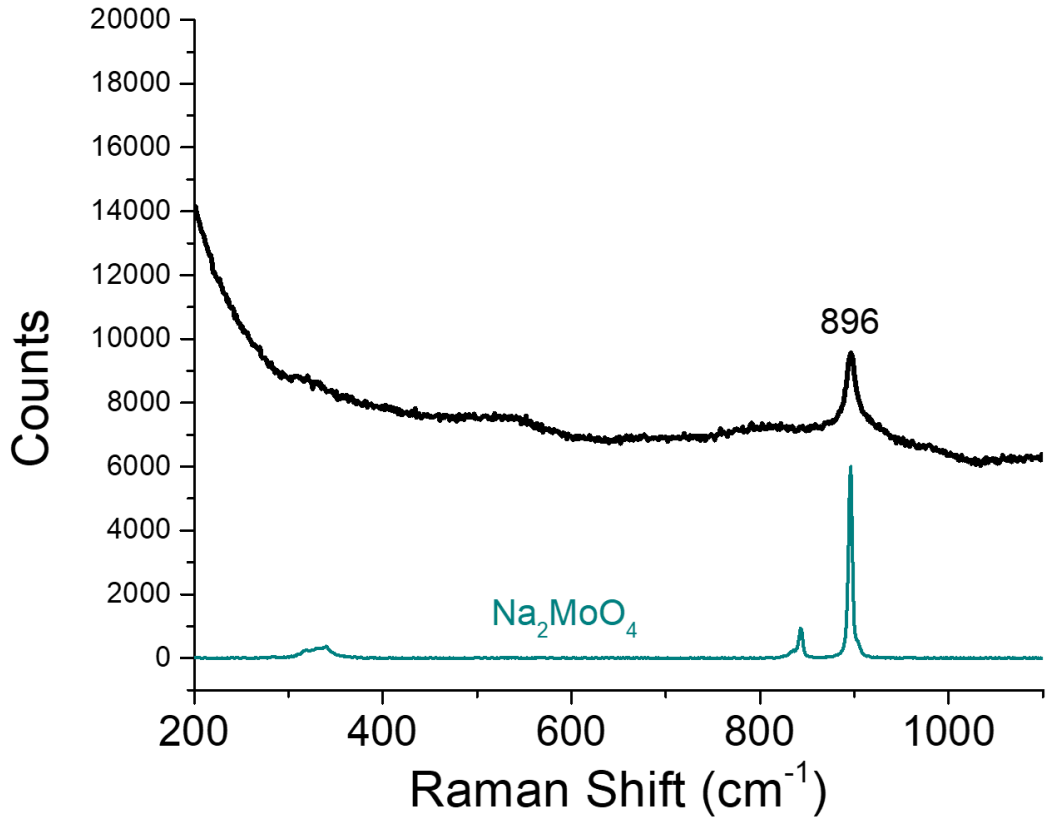

SI Figure 5. Raman spectroscopy of the solution following reaction between ZnO:MoO_3 in water and filtering the precipitate. A spectrum of solid Na_2MoO_4 is provided as a standard.

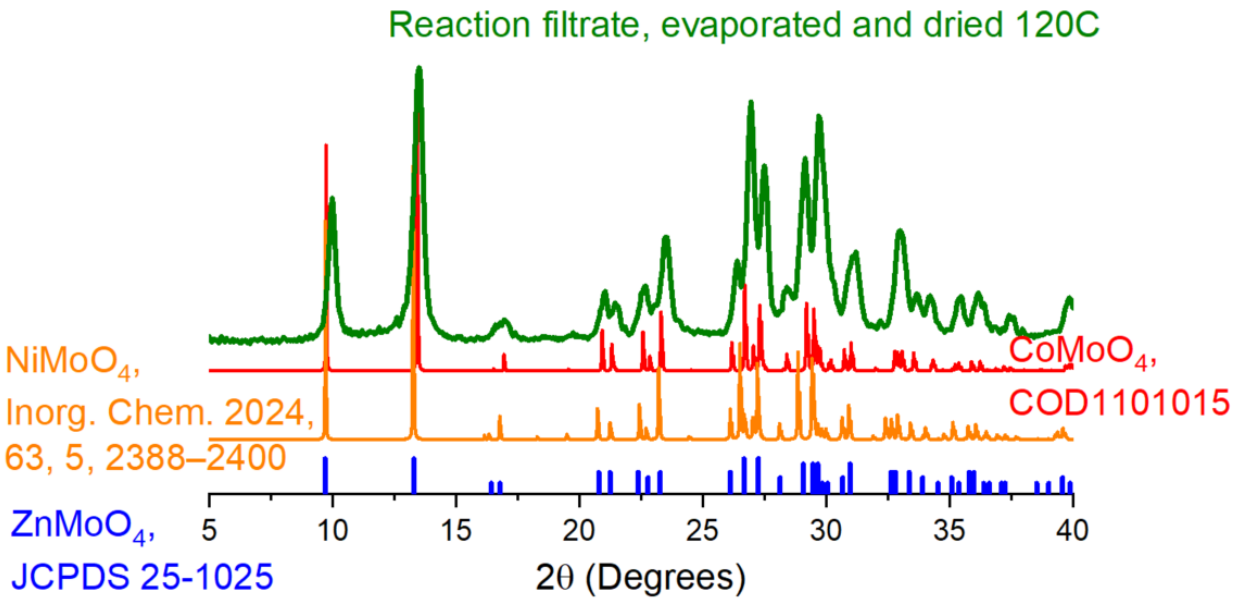

SI Figure 6. PXRD of the residue obtained by evaporating the filtrate from which **1** precipitates (green). This matches $ZnMoO_4 \bullet 0.8H_2O$, JCPDS 25-1025 (blue). Notably, there is no structural solution for this phase currently, but it is likely close to reported analogs $CoMoO_4 \bullet 0.8H_2O$ and $NiMoO_4 \bullet 0.6H_2O$.

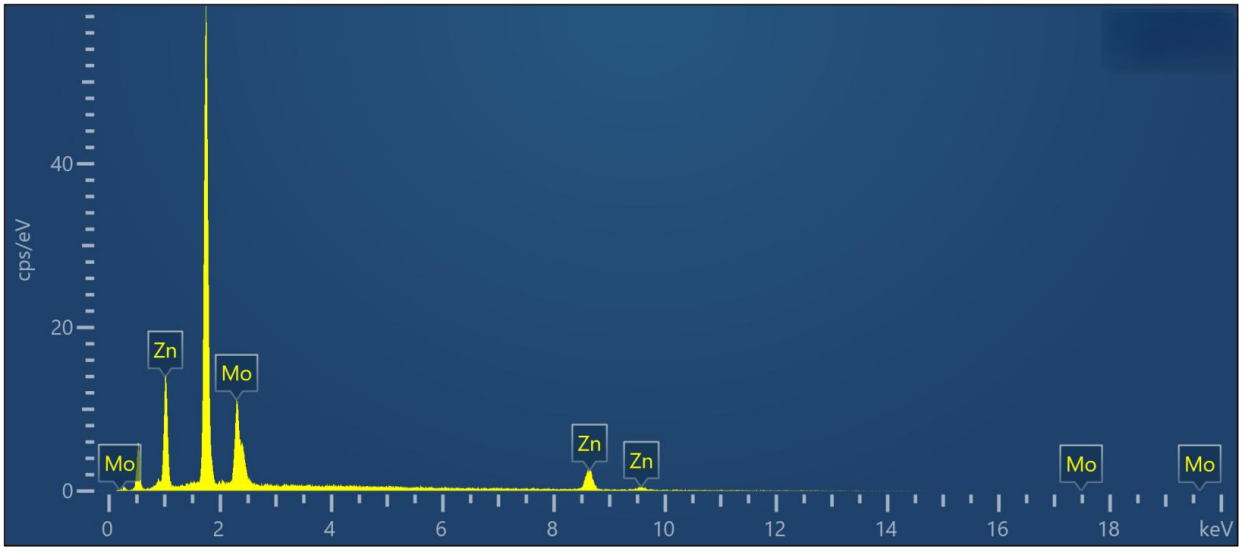

Element	Line Type	wt%	Wt % Sigma	At%
Zn	L-line series	49.29	0.99	58.79
Mo	L-line series	50.71	0.99	41.21
Total		100.00		100.00

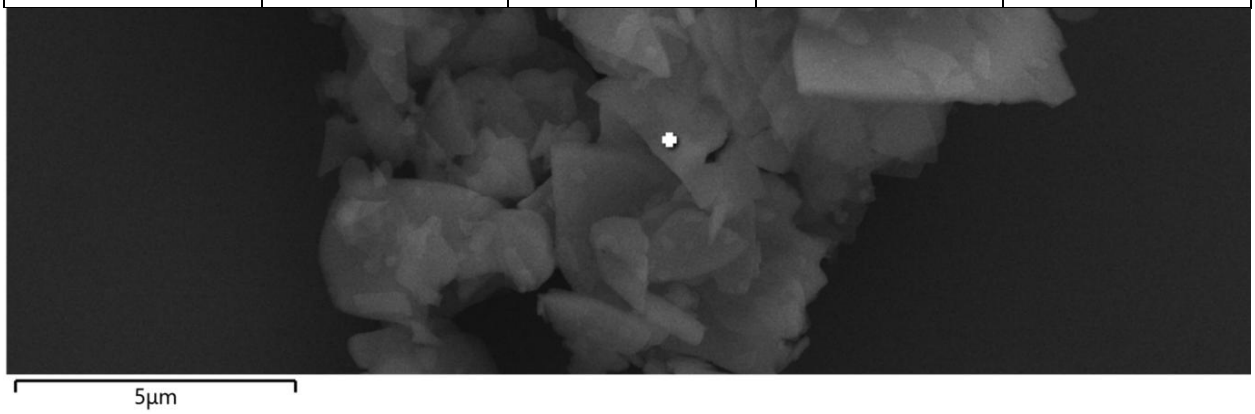

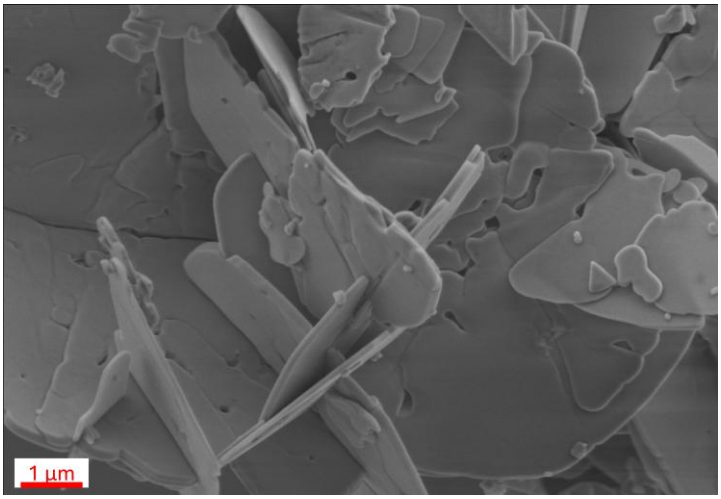

SI Figure 7. SEM/EDS analysis for **1** showing plate-like morphology.

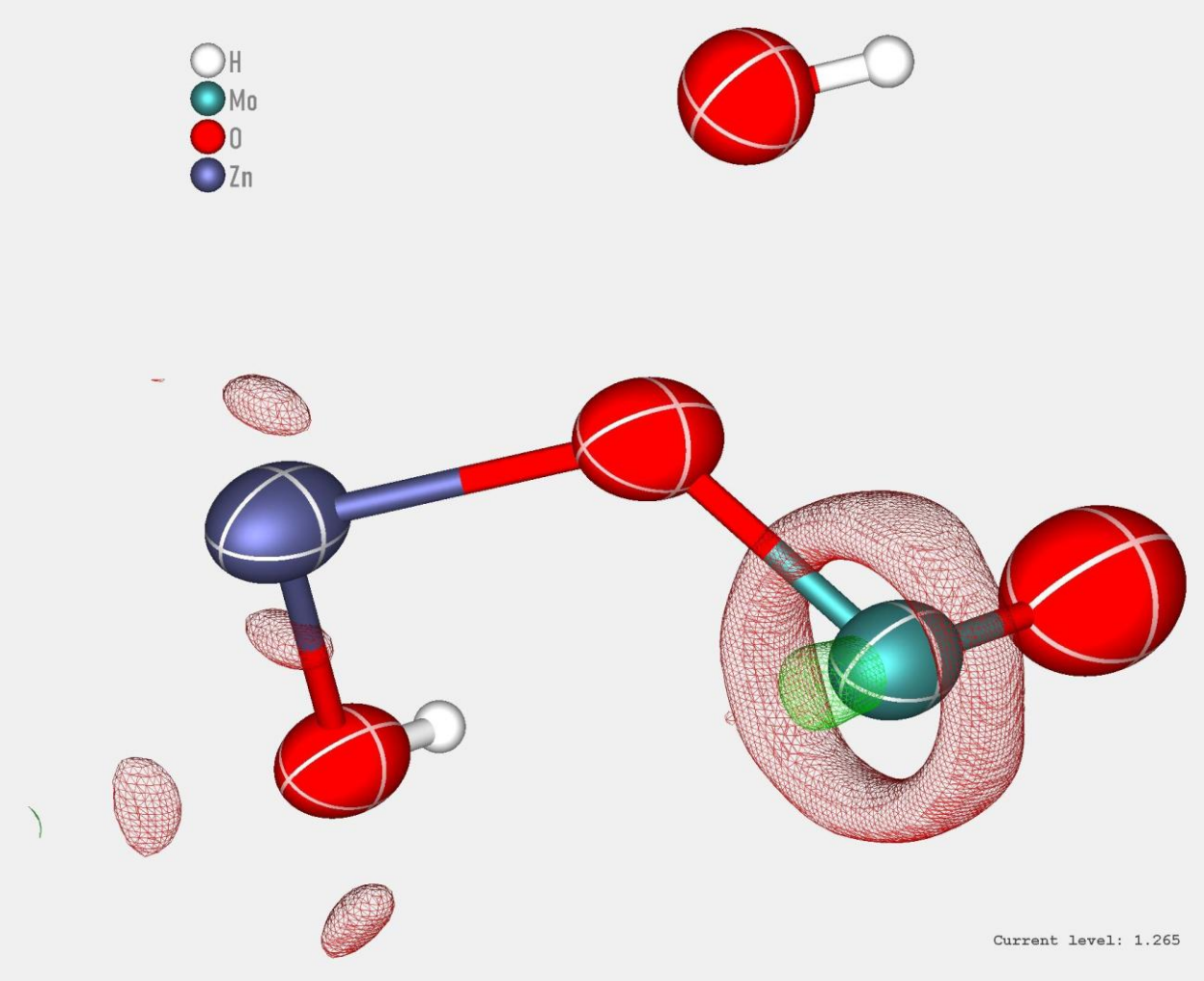

SI Figure 8. ORTEP-style drawing with the residual electron density.

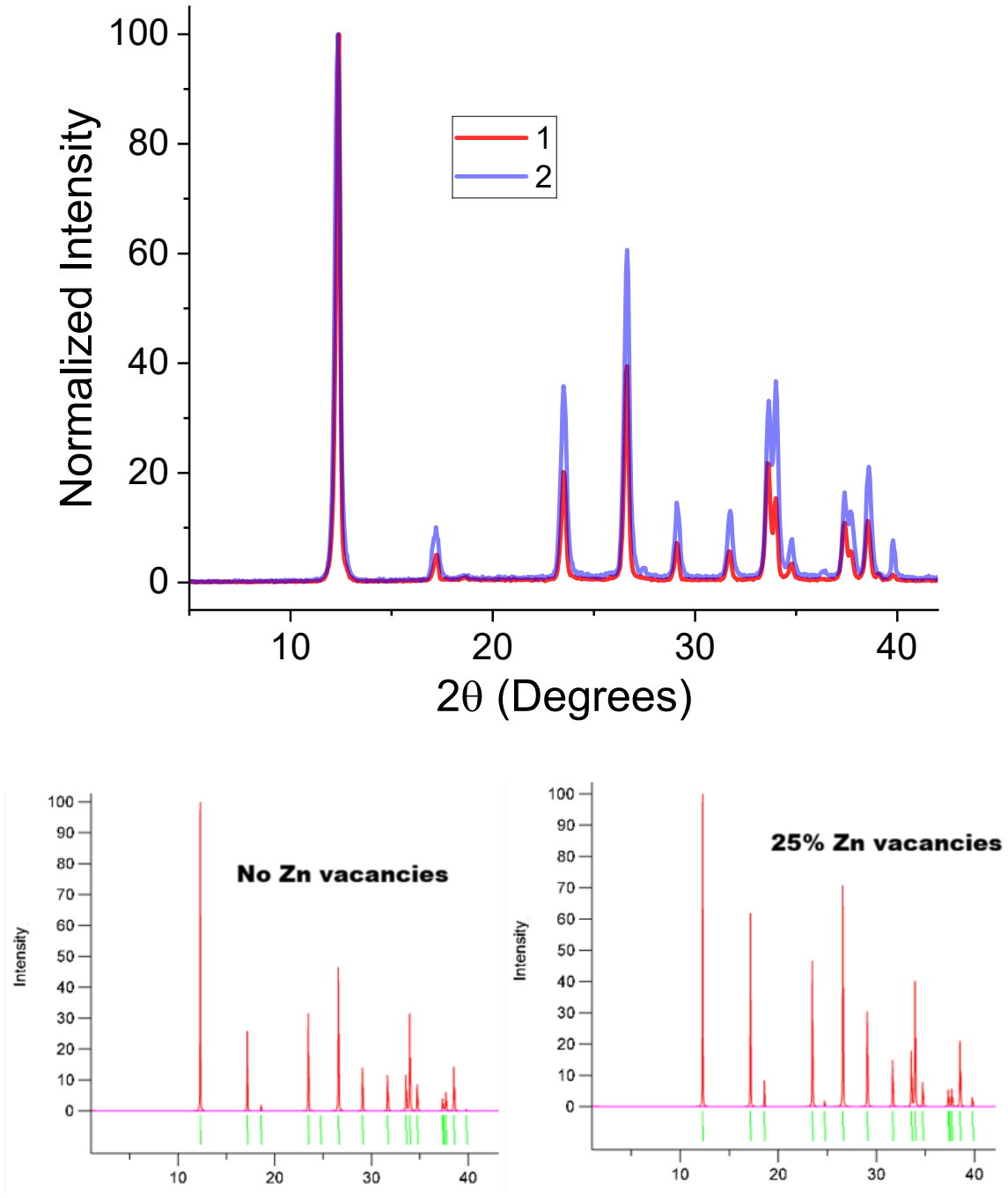

SI Figure 9. (Top) Normalized PXRD data for samples of **1** and **2.** (Bottom) Simulated PXRD data for **1** having full Zn occupancy (left) and 25% Zn vacancies (right), showing different relative intensities for peaks relative to the major peak at 12.3°.

SI Table 1: Parameters from Neutron Diffraction Refinement. *refined anisotropically

space group				$R\bar{3}m$ (#166)		
Z				3		
Temperature, K				298		
a (Å)				6.142		
c (Å)				21.589		
V (Å^3)				705.39		
R_p, R_{wp}, R_{exp}, χ^2				0.016, 0.021, 0.011, 3.561		
Radiation				1.5 Å		
Atomic Coordinates and Occupancies						
Atom	*x*	*y*	*z*	*Wyck*	*Occ*	U_{iso}/U_{eq}
Mo	0	0	0.4154	6*c*	1	0.051*
Zn	0.5	0	0.5	9*e*	0.92	0.041*
O_{water}	0	0	0	3*b*	1	0.063
O_{Mo_ap}	0	0	0.3353	6*c*	1	0.094
O3	0.4927	0.5073	0.2214	18*h*	1	0.053
O4	0	0	0.2116	6*c*	1	0.043
Hydrogens						
Atom	*x*	*y*	*z*	*Wyck*	*Occ*	U
H_{water}	0.5954	0.4046	0.3014	18*h*	0.333	0.096
H4	0	0	0.2556	6*c*	1	0.070
Hx	0	0	0.1652	6*c*	0.23	0.100

XFEL Microcrystal Diffraction

The structure of $(H_2O)Zn_3(OH)_2(MoO_4)_2$ was determined by serial femtosecond diffraction at the MFX endstation of the Linac Coherent Light Source (LCLS) under the Mail-In Structural Science program.

All data were collected under LCLS experiment number mfx101232725 in January, 2026. The X-ray photon energy was 14.93 keV with a per-pulse power density of ~1.2 mJ. Sample delivery was performed using the purpose built LCLS fast fixed-target stage endstation inspired by previous work [1][2][3]. 3-D printed 24-well sample chips were raster scanned through the x-ray beam with 30 micron spacings between shots allowed for synchronization to the 120 Hz repetition rate of the FEL and total collection of 70,000 shots per sample well. Samples were thoroughly dispersed in Molykote® high vacuum grease at a concentration of 20 mg powder/1 g grease and spread thinly on a Kapton support using a 3-D printed plastic scraper. Diffraction patterns were recorded at 120 Hz on a JUNGFRAU 16M detector [4] at a sample-detector distance of 85 mm.

Unit cells were determined by three methods. Method 1: cells determined from synthetic powder diffraction patterns following the methods of Schriber, Paley, et al.[5] and using TOPAS-Academic[6] for indexing. Method 2: Synthetic powder patterns[5] indexed by an open-source implementation of the SVD-Index algorithm with starting guesses initialized by a machine learning model[7]. Method 3: cells determined using the experimental Findexer technique[8] on scattering vector pairs and the angles between them. Method 3 was the primary approach because it uses three-dimensional spot relationships and therefore is more accurate and reliable. For cases where spot-pair angle distributions were unresolved, (e.g. samples consisting primarily of multicrystal clumps), then methods 2 and 1 were used as fallbacks. Note that none of these methods allow conventional error propagation to the derived cell parameters; therefore we are unable to give estimated uncertainties on the cell dimensions.

Indexing, integration, and merging were performed in *cctbx.xfel.small_cell_process*[9] and *cctbx.xfel.merge*[10] using the *DIALS* framework[11] and published methods for small-molecule serial data[5,12]. Subsequent structure solution and refinement were typically performed in ShelXT and ShelXL[13,14] with the aid of Olex2[15] and Platon[16].

Since the Findexer method has not been published in full, we give a few more details here. Briefly, we measure triplets (q1, q2, theta) for every pairwise combination of two spots in the dataset. These spot pairs are embedded in a three-dimensional space of two lengths and one angle. We harvest 500 high-density points in this space using clustering or peakfinding. Next, we use the fact that every spot pair is also present in the

underlying reciprocal lattice. From every harvested spot pair we generate a two-dimensional sublattice, which is always possible because two lengths and one angle define a 2d lattice. The sublattice that explains the greatest number of observed spot pairs (often around 10% of the total) is selected as an "anchor" sublattice. The three-dimensional lattice is completed by selecting two additional half-indexed spot pairs in which one (common) side is unindexed by the sublattice and the two (distinct) other sides are indexed. This procedure gives the three additional unknown parameters of the 3d lattice: one length, of the common unindexed side, and two angles, with the two distinct indexed sides. Finally, doubled and tripled cell multiples are tested, in case one of the previous steps identified a higher-order lattice vector. This method will be described fully in an upcoming publication.

Verification of unit cell candidates is empirical, based on indexing and structure solution. Since the *small_cell* indexing method [9] requires a previously determined cell, generally an incorrect cell proposal will fail at the indexing stage. If indexing is performed in a wrong but related cell (for example a half-volume subcell) then the structure solution may fail or give a chemically unreasonable result. In one notable example, a structural family was described in C-centered lattices by XFEL diffraction [5] and later recharacterized in the corresponding primitive sublattices by single-crystal diffraction [17]. Recent XFEL experiments benefit from higher-energy photons and advanced indexing techniques; however, in view of the challenges of lattice determination, we note that XFEL structures must always be evaluated carefully at the solution and refinement stages.

[1]Roedig, P. *et al*. High-speed fixed-target serial virus crystallography. *Nat Methods* **14**, 805–810 (2017).

[2]Doak, R. B. *et al*. Crystallography on a chip – without the chip: sheet-on-sheet sandwich. *Acta Cryst D* **74**, 1000–1007 (2018).

[3]Saha, S. *et al*. Scalable fabrication of an array-type fixed-target device for automated room temperature X-ray protein crystallography. *Sci Rep* **15**, 334 (2025).

[4] Mozzanica, A., Andrä, M., Barten, R., Bergamaschi, A., Chiriotti, S., Brückner, M., Dinapoli, R., Fröjdh, E., Greiffenberg, D., Leonarski, F., Lopez-Cuenca, C., Mezza, D., Redford, S., Ruder, C., Schmitt, B., Shi, X., Thattil, D., Tinti, G., Vetter, S., & Zhang, J. (2018). The JUNGFRAU detector for applications at synchrotron light sources and XFELs. *Synchrotron Radiation News* **31**, 16-20. doi: 10.1080/08940886.2018.1528429

[5] Schriber, E. A., Paley, D. W., Bolotovsky, R., Rosenberg, D. J., Sierra, R. G., Aquila, A., Mendez, D., Poitevin, F., Blaschke, J. P., Bhowmick, A., Kelly, R. P., Hunter, M., Hayes, B., Popple, D. C., Yeung, M., Pareja-Rivera, C., Lisova, S., Tono, K., Sugahara, M., Owada, S.,

Kuykendall, T., Yao, K., Schuck, P. J., Solis-Ibarra, D., Sauter, N. K., Brewster, A. S., & Hohman, J. N. (2022). Chemical crystallography by serial femtosecond X-ray diffraction. *Nature* **601**, 360-365. doi: 10.1038/s41586-021-04218-3

[6] Coelho, A. A. (2018). TOPAS and TOPAS-Academic: An optimization program integrating computer algebra and crystallographic objects written in C++. *J. Appl. Cryst.* **51**, 210-218. doi: 10.1107/S1600576718000183

[7] Mittan-Moreau, D. W., Oklejas, V., Paley, D. W., Hofgard, E., Mansouri Tehranii, A., Smidt, T., & Brewster, A. S. (2026). ML-Index: A data-driven approach to powder diffraction indexing. *J. Appl. Cryst.*, In review.

[8] Daniel Paley, Aaron Brewster, David Mittan-Moreau, Nicholas Sauter (2025). FINDEXER: a new technique to find unit cells in sparse serial patterns. *Struct. Dyn.* **12**, A266. doi: 10.1063/4.0001055

[9] Brewster, A. S., Sawaya, M. R., Rodriguez, J., Hattne, J., Echols, N., McFarlane, H. T., Cascio, D., Adams, P. D., Eisenberg, D. S., & Sauter, N. K. (2015). Indexing amyloid peptide diffraction from serial femtosecond crystallography: New algorithms for sparse patterns. *Acta Cryst.* **D71**, 357-366. doi: 10.1107/S1399004714026145

[10] Brewster, A. S., Paley, D. W., Bhowmick, A., Mittan-Moreau, D. W., Young, I. D., Mendez, D. A., Tchoń, D. M., Poon, B. K., & Sauter, N. K. (2025). cctbx.xfel: a suite for processing serial crystallographic data. *bioRxiv* (preprint). doi: 10.1101/2025.05.04.652045

[11] Winter, G., Waterman, D. G., Parkhurst, J. M., Brewster, A. S., Gildea, R. J., Gerstel, M., Fuentes-Montero, L., Vollmar, M., Michels-Clark, T., Young, I. D., Sauter, N. K., & Evans, G. (2018). DIALS: Implementation and evaluation of a new integration package. *Acta Cryst.* **D74**, 85-97. doi: 10.1107/S2059798317017235

[12] Aleksich, M., Paley, D. W., Schriber, E. A., Linthicum, W., Oklejas, V., Mittan-Moreau, D. W., Kelly, R. P., Kotei, P. A., Ghodsi, A., Sierra, R. G., Aquila, A., Poitevin, F., Blaschke, J. P., Vakili, M., Milne, C. J., Dall'Antonia, F., Khakhulin, D., Ardana-Lamas, F., Lima, F., Valerio, J., Han, H., Gallo, T., Yousef, H., Turkot, O., Bermudez Macias, I. J., Kluyver, T., Schmidt, P., Gelisio, L., Round, A. R., Jiang, Y., Vinci, D., Uemura, Y., Kloos, M., Hunter, M., Mancuso, A. P., Huey, B. D., Parent, L. R., Sauter, N. K., Brewster, A. S., & Hohman, J. N. (2023). XFEL microcrystallography of self-assembling silver n-alkanethiolates. *J. Am. Chem. Soc.* **145**, 17042–17055. doi: 10.1021/jacs.3c02183

[13] Sheldrick, G. M. (2015). SHELXT — Integrated space-group and crystal-structure determination. *Acta Cryst.* **A71**, 3–8. doi: 10.1107/S2053273314026370

[14] Sheldrick, G. M. (2015). Crystal structure refinement with SHELXL. *Acta Cryst.* **C71**, 3–8. doi: 10.1107/S2053229614024218

[15] Dolomanov, O. V., Bourhis, L. J., Gildea, R. J., Howard, J. A. K., & Puschmann, H. (2009). OLEX2: A complete structure solution, refinement and analysis program. *J. Appl. Cryst.* **42**, 339–341. doi: 10.1107/S0021889808042726

[16] Spek, A. L. (2003). Single-crystal structure validation with the program PLATON. *J. Appl. Cryst.* **36**, 7-13. doi: 10.1107/S0021889802022112

[17] Lee, W. S., Müller, P., Samulewicz, N., Deshpande, T., Wan, R., Tisdale, W. A. (2024). Synthesis and Structural Anisotropy of Single-Crystalline 2D AgEPh (E = S, Se, Te). Chem. Mater. 36, 9904-9913.

Electronic Structure Calculations

Local density approximation (LDA) total energy and structural optimization calculations were performed using the Vienna Ab initio Simulation Package (VASP). [1-2] The Perdew-Burke-Ernzerhof generalized gradient approximation (PBE-GGA) [3] was applied to the projector augmented-wave (PAW) [4] pseudopotentials within VASP. The pseudopotentials used were PBE.54 with titles of PAW_PBE Mo, PAW_PBE Zn, PAW_PBE O, and PAW_PBE H, for molybdenum, zinc, oxygen, and hydrogen respectively. The linear tetrahedron method was used for reciprocal space integrations [5] over a Monkhorst-Pack K-point mesh [6] of 11 x 11 x 3 and the conjugate algorithm was used with an energy cut off of 500 eV.

[1] G. Kresse, J. Hafner: Phys Rev B 47 (1993) 558–561.

[2] G. Kresse, J. Furthmüller: Phys Rev B 54 (1996) 11169–11186.

[3] J.P. Perdew, K. Burke, Y. Wang: Phys Rev B 54 (1996) 16533–16539.

[4] P.E. Blöchl, Phys Rev B 50 (1994) 17953–17979.

[5] P.E. Blöchl, O. Jepsen, O.K. Andersen: Phys Rev B 49 (1994) 16223–16233.

[6] H.J. Monkhorst, J.D. Pack: Phys Rev B 13 (1976) 5188–5192.